Observational Study of a Multiple Microburst-Producing Storm Part I: Kinematic, Dynamic and Thermodynamic Structures

YEONG-JER LIN,[1]　WILLIAM E. MCNAMEE[2]　AND　JOHN A. COOVER, JR.[2]

ABSTRACT

Some kinematic, dynamic, and thermodynamic structures of a multiple microburst-producing storm, which occurred on 5 August 1982 in Colorado, were studied for three analysis times at 1845, 1847, and 1850 MDT. Dual Doppler data collected during the project of Joint Airport Weather Studies (JAWS) at Denver's Stapleton International Airport were objectively analyzed to produce a three-dimensional wind field. The domain of interest had a horizontal dimension of 15 km by 15 km covering three microbursts. There were five analysis levels in the vertical ranging from 0.25 to 1.25 km AGL. The horizontal and vertical grid spacings were 0.5 and 0.25 km, respectively. Vertical velocities were computed by integrating the anelastic continuity equation upward from the surface. Subsequently, fields of deviation perturbation pressure and temperature were recovered from a detailed wind field using the three momentum equations. These fields were then subjected to internal consistency checks to determine the level of confidence before interpretation.

Results show that the microbursts being investigated are embedded within the high-reflectivity cores with heavy precipitation. A wet microburst is accompanied by the misocyclone at levels above 0.75 km in the downdraft. It has the slowly descending downflow forming a cold core at the lowest levels due to the evaporation of raindrops. Near the gust front (GF), a mesocyclone-like circulation develops in the area where the warm, dry environmental air interacts with the negatively buoyant microburst outflow. High pressure forms inside the microburst core with low pressure in the strong wind regions. Pronounced horizontal pressure gradients occur from the microburst center outward to balance the strong diverging outflow that region. The retrieved pressure and temperature fields agree well with the storm's kinematic structure. The combined effects of misocyclone circulations, perturbation pressure gradients, buoyancy and precipitation loading are responsible for maintaining the microburst downdrafts in the atmospheric boundary layer (ABL).

---

[1]　*Department of Earth and Atmospheric Science, Saint Louis University, U. S. A.*

[2]　*Present affiliation: Air Weather Service, U. S. Air Force.*

1. INTRODUCTION

In the Doppler study by Wilson *et al*. (1984), a microburst is defined as a downdraft-induced, damaging horizontal flow near the surface, whose horizontal dimension is less than 4 *km*, and whose differential velocity is greater than 10 *m/s*. Using the dual-Doppler data collected during the Joint Airport Weather Studies (JAWS) project, Lin *et al*. (1987) and Lin and Hughes (1987) investigated the kinematic, dynamic, and thermodynamic structures of a microburst-producing thunderstorm which occurred on 14 July 1982 in Colorado. This storm produced a single microburst with considerable intensity. Dual-Doppler data collected from 1646 to 1648 MDT (mountain daylight time) were analyzed to produce a three-dimensional wind field. The thermodynamic retrieval method of Gal-Chen (1978) was then employed to recover fields of deviation perturbation pressure and temperature. Results showed that the microburst being investigated was embedded within the high-reflectivity region with heavy precipitation. A strong downflow impinged on the surface, producing a stagnation mesohigh pressure area inside the microburst. This mesohigh was accompanied by low pressure in the strongest outflow regions, forming a pronounced horizontal perturbation-pressure gradient outward from the high pressure center. Such pressure patterns were in good agreement with the surface observations in similar cases for two different storms. The outflow regions extended from the surface to approximately 1 *km* height with maximum divergence in excess of 10^{-2} s^{-1}. The outflow air was negatively buoyant due to evaporation in the outskirt of the microburst. The microburst had a warm-cored structure, as compared to the environmental virtual temperature, due to a strong downflow embedded within the wet environment. The retrieved buoyancy field agreed well with the updraft-downdraft structure with warming in the updrafts and cooling in the downdrafts. The combined effects of perturbation-pressure gradients, buoyancy and precipitation loading were responsible for maintaining vigorous convection of the downdrafts which produced the strong diverging outflow at low levels.

The purpose of this study is to investigate, via a retrieval method, the kinematic, dynamic, and thermodynamic structures of a multiple microburst-producing thunderstorm, which occurred on 5 August 1982 in Colorado. Unlike the 14 July case which produced only a single microburst, the 5 August case produced multiple microbursts (more than two), within a domain comparable to the 14 July 1982 case, during the storm's life time. For comparison, the previously studied case (14 July) is called the simple case, while the case under investigation (5 August) is referred to as the complex case hereafter. Dual-Doppler data collected at 1845, 1847, and 1850 MDT analysis times were objectively analyzed to produce a three-dimensional wind field. The domain of interest had a horizontal dimension of 15 *km* by 15 *km* with five levels in the

vertical. Because of the shallow volume scans, dual-Doppler data were available only in the layer from the surface to 1.25 *km*, covering the atmospheric boundary layer (ABL). Vertical velocities were computed by integrating the anelastic continuity equation upward from the surface. Subsequently, fields of deviation perturbation pressure and virtual temperature were recovered from the derived winds using the three momentum equations. These retrieved fields, together with the observed wind field, were then employed to investigate certain important structural features and momentum and kinetic energy budgets of the storm, which produced multiple microbursts in the ABL.

In Part I of this study, emphasis is placed on the kinematic, dynamic and thermodynamic structures of the complex case. A description of the data is given in Section 2. In Section 3, computational procedures are presented. This is followed by the discussion of results in Section 4. Finally, Section 5 presents the conclusions.

2. THE DATA

The synoptic situation at 0600 MDT 5 August 1982 featured a low pressure system in southwest Kansas and southeast Montana (Fig. 1). A quasi-
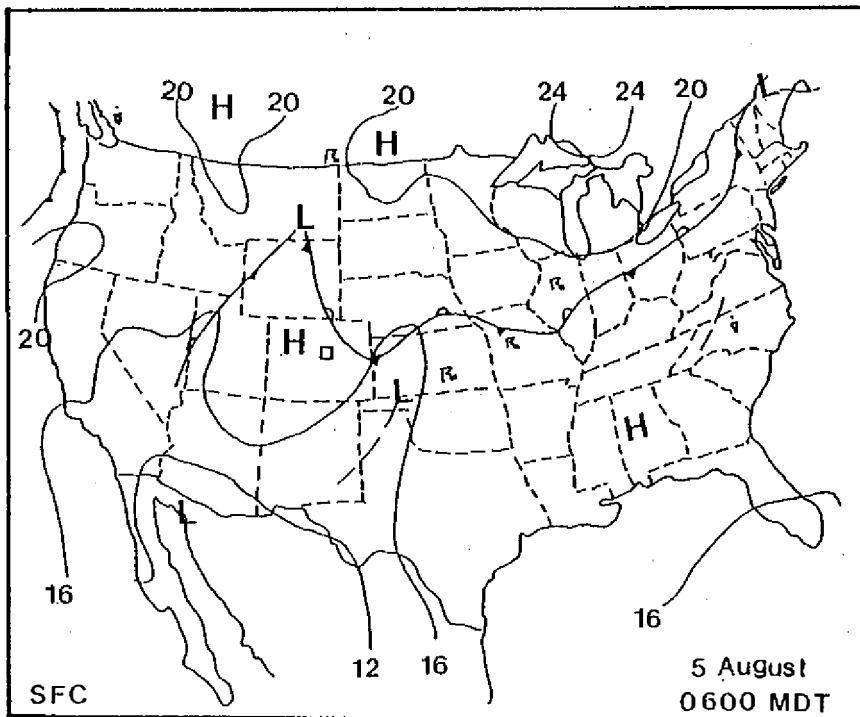

Fig. 1. The surface synoptic map at 0600 MDT 5 August 1982. The small box located in the state of Colorado indicates the JAWS area.

stationary front connected the low pressure centers and bisected northeast Colorado. The front moved slowly northeast during the day. The surface forcing and upper-level dynamics were very weak on this day with the jet stream located from Oregon through Idaho and finally existing the United States through northeast Montana. The Denver sounding for 1800 MDT 5 August 1982 (Fig. 2) features a well-mixed boundary layer extending to 1.5 km above ground level (AGL). The lifting condensation level (LCL) is 650 mb (2 km), which is much lower than that reported in Lin *et al.* (1987) for the simple case (approximately at 3.5 km), see their Fig. 1. Note the unusual depth of the moist layer (4 ~ 7 km) for a high plains storm and the general lack of mid-level dry air. A cross-comparison between the sounding for 14 July (simple case) and that for 5 August (complex case) reveals different characteristics. The simple case had a much lower mixing ratio (4.5 g/kg), a shallow moist layer (1.5 km) and little directional shear in the ABL. Conversely, the complex case had relatively high mixing ratio (6.5 g/kg), a deeper moist layer (3 km), and winds backing sharply with height below 3 km. Further, both soundings exhibited conditional
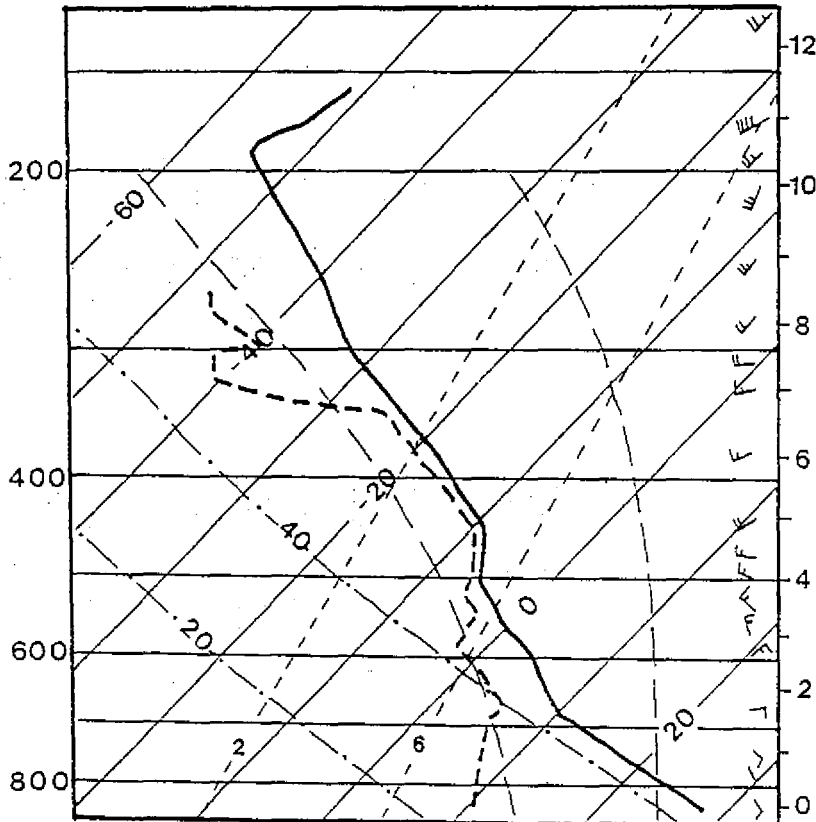

Fig. 2.   The Denver sounding release at 1800 MDT 5 August 1982. Heights are in kilometers AGL.

instability with little lift required or increase of temperature necessary to induce convection.

Dual-Doppler data, obtained from CP-3 and CP-4 centered at 1845, 1847, and 1850 MDT, were considered in this study. A JAWS network and the computational domain are displayed in Fig. 3. At the times of analyses, the microbursts and the parent storm were nearly stationary. Some kinetic aspects of this storm were reported in Elmore *et al.* (1987) using the reduced domain. The data were strictly checked to meet the prespecified criteria. Folded data were corrected and ground clutters were removed. Only those data with a high signal-to-noise ratio were accepted for analysis in each slab. All variables within a slab were interpolated onto horizontal Cartesian grids (31×31), with a grid spacing of 0.5 km using a 1.75 km scan radius. There were five equally spaced analysis levels in the vertical ranging from 0.25 to 1.25 km.
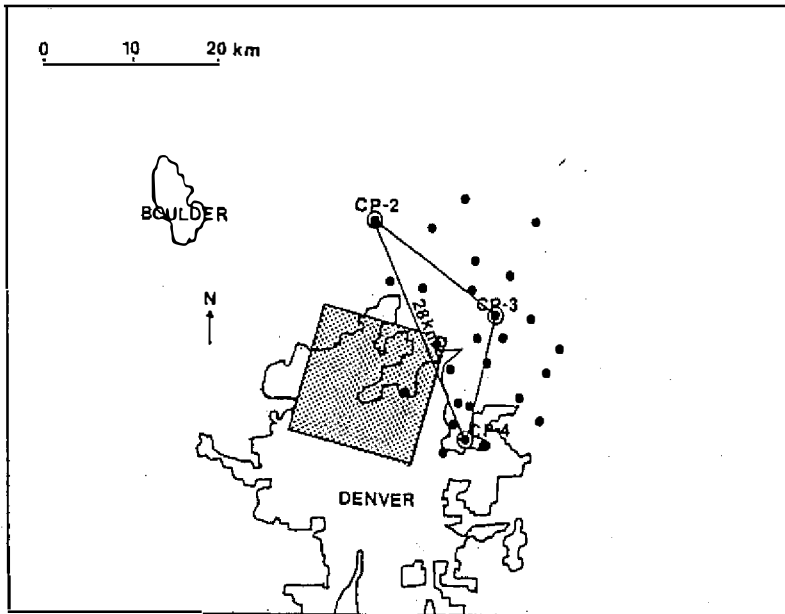

Fig. 3. A JAWS network showing the locations of three NCAR Doppler radars, CP-2, CP-3, and CP-4, and 27 PAM stations (solid dot). The shaded box represents the domain of interest (15 km by 15 km).

3. COMPUTATIONAL PROCEDURES

We employed the method suggested by Armijo (1969) to derive the horizontal wind components (u, v) from two radial velocity equations, the anelastic continuity equation, and an empirical formula of terminal fall speed. For detail, see studies by Lin *et al.* (1987) and Lin and Hughes (1987). Vertical veloci-

ties (w) were computed from the anelastic continuity equation by integrating upward from the surface assuming $w = 0$ at the surface.

The derived wind field is subject to both random and non-random errors. Using the technique similar to that of Wilson *et al*. (1984), an error analysis was conducted. Our finding shows that the combined errors due to statistical uncertainty in the radial velocity estimates and geometrical considerations are approximately $1 \sim 2 \ m/s$ for the horizontal-derived winds. For vertical velocity calculation, the uncertainty in the w estimate is more difficult to determine since it is closely related to errors in horizontal divergence, boundary conditions, etc. Using the real storm Doppler data, Nelson and Brown (1987) showed that the accuracy of w is generally within 10% in the area with maximum updraft/downdraft speed. Once the detailed wind field was derived, fields of deviation perturbation pressure and virtual temperature from their horizontal averages were retrieved from the three momentum equations (Gal-Chen, 1978).

The momentum equations in a moving coordinate system can be written as

$$\frac{\partial p'}{\partial x} = -\rho_0 \frac{Du}{Dt} + f_1 = F \tag{1}$$

$$\frac{\partial p'}{\partial y} = -\rho_0 \frac{Dv}{Dt} + f_2 = G \tag{2}$$

$$\rho' g + \frac{\partial p'}{\partial z} = -\rho_0 \frac{Dw}{Dt} + f_3 = H \tag{3}$$

where the prime represents the perturbation quantity; Du/Dt, Dv/Dt, and Dw/Dt are accelerations along the x-, y-, and z-axes, respectively; f_i ($i = 1, 2, 3$) denotes the forces other than the pressure gradient force per unit volume; and other symbols have their conventional meanings.

In the preceding equations, the precipitation drag term in f_i was estimated from the rainwater mixing ratio, q_r, by relating q_r empirically to radar reflectivity. The frictional term was formulated based on the parameterization of Klemp and Wilhelmson (1978). For details, see Lin *et al*. (1987).

The horizontal perturbation-pressure equation at a given level was derived from (1) and (2) to yield

$$\frac{\partial^2 P'}{\partial x^2} + \frac{\partial^2 P'}{\partial y^2} = \frac{\partial F}{\partial x} + \frac{\partial G}{\partial y} \tag{4}$$

Equation (4) was solved by successive overrelaxation (SOR) with the Neumann boundary condition. The unique solution of Eq. (4) exists only if the horizontal average of P', denoted by $\langle P' \rangle$, is removed from P' in Eq. (4).

Once the field of deviation perturbation pressure (P_d') is obtained, the deviation virtual temperature field (T_{vd}') can be calculated from the buoyancy equation, i.e.,

$$T_{vd}' = \frac{\overline{T_v}}{g} \left\{ \underbrace{\left(\frac{Dw}{Dt} - \left\langle \frac{Dw}{Dt} \right\rangle \right)}_{\text{VAC}} + \underbrace{\frac{1}{\rho_0} \frac{\partial P_d'}{\partial z}}_{\text{VPG}} + \underbrace{g(q_r - \langle q_r \rangle)}_{\text{RWL}} - \underbrace{(F_z - \langle F_z \rangle)}_{\text{VFF}} \right\} \quad (5)$$

where terms VAC, VPG, RWL, and VFF represent the contributions of vertical acceleration, vertical perturbation-pressure gradient, rainwater loading, and friction, respectively, to T_{vd}'. The retrieved temperature represents a virtual cloud temperature since it accounts for both deviation of virtual temperature perturbation and cloud water content (Roux *et al.*, 1984).

It must be pointed out that only under error-free conditions are the deduced horizontal pressure gradients in exact balance with the right-hand side of Eqs. (1) and (2). But for real storm data, P' is a least-squares solution. Gal-Chen and Hane (1981) proposed a measure of the relative error, E_r, in pressure retrieval, defined as

$$E_r \equiv \frac{\int\int \left\{ \left(\frac{\partial p'}{\partial x} - F \right)^2 + \left(\frac{\partial p'}{\partial y} - G \right)^2 \right\} dxdy}{\int\int (F^2 + G^2) dxdy} \quad (6)$$

This relationship is necessary but not sufficient. Thus, E_r should only be considered as a relative measure of "goodness" of fit of the perturbation-pressure gradients and the known functions F and G. It is also necessary to examine the physical consistency of thermodynamic variables with respect to the storm's kinematic structure at the analysis time.

4. DISCUSSION OF RESULTS

The kinematic structure of the 5 August 1982 case was reported in Elmore *et al.* (1986) using the reduced domain ($4.5 \ km \times 4.5 \ km$) centered at microburst M1. The objective analysis employed was the Cressman (1959) interpolation scheme with an influence radius equal to the grid spacing of 150 m. They used the 150 m horizontal grid spacing to calculate fields of convergence/divergence and vertical velocity starting from the lowest level near 50 m AGL. Results showed that strong downward motion up to 10 m/s occurs inside the microburst.

Unlike the kinematic study by Elmore *et al.* (1986), our study is focused on the dynamic and thermodynamic study of a microburst-producing storm via a thermodynamic retrieval method. As noted earlier, this type of study requires first, second and third derivatives in velocity. Therefore, the wind field

must be much smoother than that for the kinematic study. We employed the Barnes (1973) type weighting function with a scan radius of 1.75 km in our objective analysis. The horizontal grid spacing was 0.5 km which is about 3.5 times larger than that of Elmore *et al.* Because of the differences in spatial resolution, objective analysis and the lowest level considered between the two studies, we expect that our results in vertical velocity will be much weaker than that reported in Elmore *et al.* (1986) for the same microburst. These points must be taken into consideration when our results are analyzed and interpreted.

4.1   Horizontal Distribution of Storm-Relative Wind and Radar Reflectivity

The derived horizontal storm-relative wind fields at 0.25, 0.75, and 1.25 km in the ABL for 1845 MDT are depicted in Fig. 4. Heights are in kilometers AGL, and distances are in kilometers from the CP-2 radar (Fig. 3). In the displays, the x-axis is directed toward 105° (E) and the y-axis is toward 15° (N). Contours of radar reflectivity in 5 dBZ increments are superimposed on the wind fields. Line AB in Fig. 4a signifies the cross section to be presented later in Figs. 10 to 11. At 0.25 km (Fig. 4a), two microbursts, M1 and M2, are observed in the highest reflectivity regions ($Z > 50\ dBZ$). The dominant microburst is the M1 feature, whose center is located at ($x = -2$, $y = -23.5$). A pronounced diverging outflow from the center of M1 is evident. Part of this outflow air moves toward the east or southeast, colliding with the northwestward environmental flow to form a gust front (GF), see the dashed line in Fig. 4a. As a result, upward motion prevails along the GF. A distinct cyclonic circulation with the center (c) located at (0, -25.5) occurs over the southern portion of the GF. Such a mesocyclone-like vortex is due to the interaction between the southeast environmental flow and the microburst outflow from the northwest, where the horizontal wind shear is maximized. It extends from the surface to 0.75 km (Fig. 4b).

Unlike M1 noted earlier, M2 does not have an apparent diverging outflow from its center, especially in the southeast part of M2. Examination of wind field reveals that the combined flow of the environmental wind, which is from the southeast at 4 m/s at this level, and the northwestward outflow from M1 almost completely overwhelms M2. It is not obvious from the horizontal wind flow that M1 and M2 are separate microbursts. However, fields of vertical velocity, perturbation and temperature deviations to be presented later confirm the presence of M2.

The horizontal wind field at 0.5 km (to be shown later) is very similar to that at 0.25 km depicted in Fig. 4a. Interesting features, e.g., the GF, microbursts M1 and M2, a mesocyclone-like vortex and the diverging outflow associated with M1, are also observed at 0.5 km. However, a dramatic change
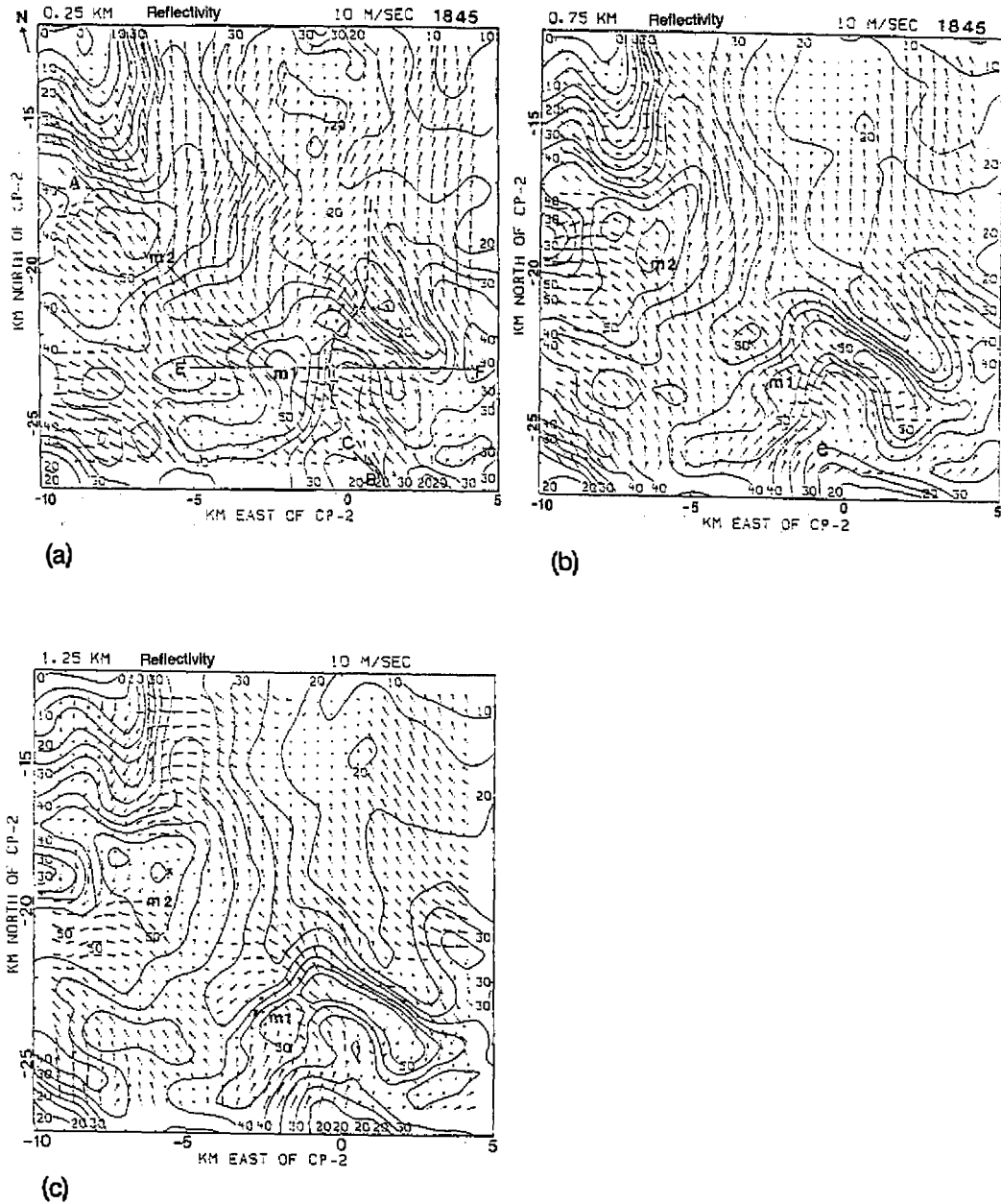
(a)

(b)

(c)

Fig. 4.   Horizontal storm-relative wind fields with reflectivity contours superimposed at (a) 0.25, (b) 0.75, and (c) 1.25 *km* for 1845 MDT. All heights are AGL. Contour interval is 5 *dBZ*. North is indicated by an arrow. Distances are in kilometers from CP-2. The dashed line represents the gust front (GF). The microburst center is labeled M1, M2, or M3, while the misocyclone center is denoted by a symbol ×. *C* represents the circulation center of a mesocyclone-like vortex. Line AB in panel (a) signifies the cross section presented in Figs. 10 to 11. At the times of analysis, the microbursts and the parent storm were almost stationary.

takes place in the horizontal wind field at 0.75 km (Fig. 4b). The flow is predominantly from the southeast or south. The dominant flow has thus become almost exclusively environmental flow in the horizontal plane with little horizontal eddying motion. The divergence field (not shown) indicates that this level is nearly nondivergent for this particular microburst-producing storm. This feature depicts a microburst diverging outflow, which is confined to the layer between the surface and 0.75 km. The GF is not apparent at this level. The cyclonic circulation center at the south end of the GF is located at $(-0.5, -25.5)$, although the circulation becomes an open wave. The cyclonic circulation extends to about 0.75 km of depth with ever increasing radius of rotation. The circulation center (c) slightly tilts to the west with height. Also note that the winds tend to blow parallel to the reflectivity contours to the northwest of M2 and to the southeast of the cyclonic circulation. This suggests that the strong outflow of precipitation cooled air from the high reflectivity core, which occurred at lower levels (Fig. 4a), is not taking place at the 0.75 km level. It also suggests that entrainment of dry environmental air from flow towards higher reflectivity values is likewise absent.

At 1.25 km (Fig. 4c), the most significant change in the wind flow as compared to that at 0.75 km is the increase in the crossing angle of environmental flow from the low reflectivity regions (southeast of M1 and northwest of M2) towards the high-reflectivity cores associated with the descending precipitation shafts. This shows that dry air entrainment occurs at this level. Note that a general cyclonic turning of the winds occurs around M1 and M2. A distinct cyclonic circulation similar to the misocyclone of Fujita (1985) occurs with M1. Its circulation center (x), located at $(-2.5, -23)$, is slightly to the west of the M1 center at 0.25 km. Inflow of dry air into M1 is from the south and southeast, while inflow into M2 is from the north. Since M1 effectively scavenges and blocks the incoming environmental wind, the M2 microburst circulation is forced to obtain its supply of dry air from the north. As this southward environmental wind meets with the northward wind near M2, a second misocyclone forms in the high reflectivity core with $Z > 50$ dBZ. The circulation center (x) is located at $(-5.5, -18.5)$ and is slightly to the northeast of the M2 center at 0.25 km. Fujita (1985) described the misocyclone's role in a microburst, enhancing precipitation loading. The two misocyclones observed in Fig. 4c, however, act as pinwheels that funnel in, and efficiently collect, dry environmental air in the $1 \sim 1.5$ km layer. As the dry air mixes with the moist downflow air in the outskirt of the downdraft, evaporative cooling prevails over that region, thereby enhancing negative buoyancy. Our temperature calculation to be presented later will support this argument.

Figure 5 shows the storm-relative wind fields at 0.25, 0.75, and 1.25 km for 1850 MDT with reflectivity contours superimposed. At 0.25 km (Fig. 5a),
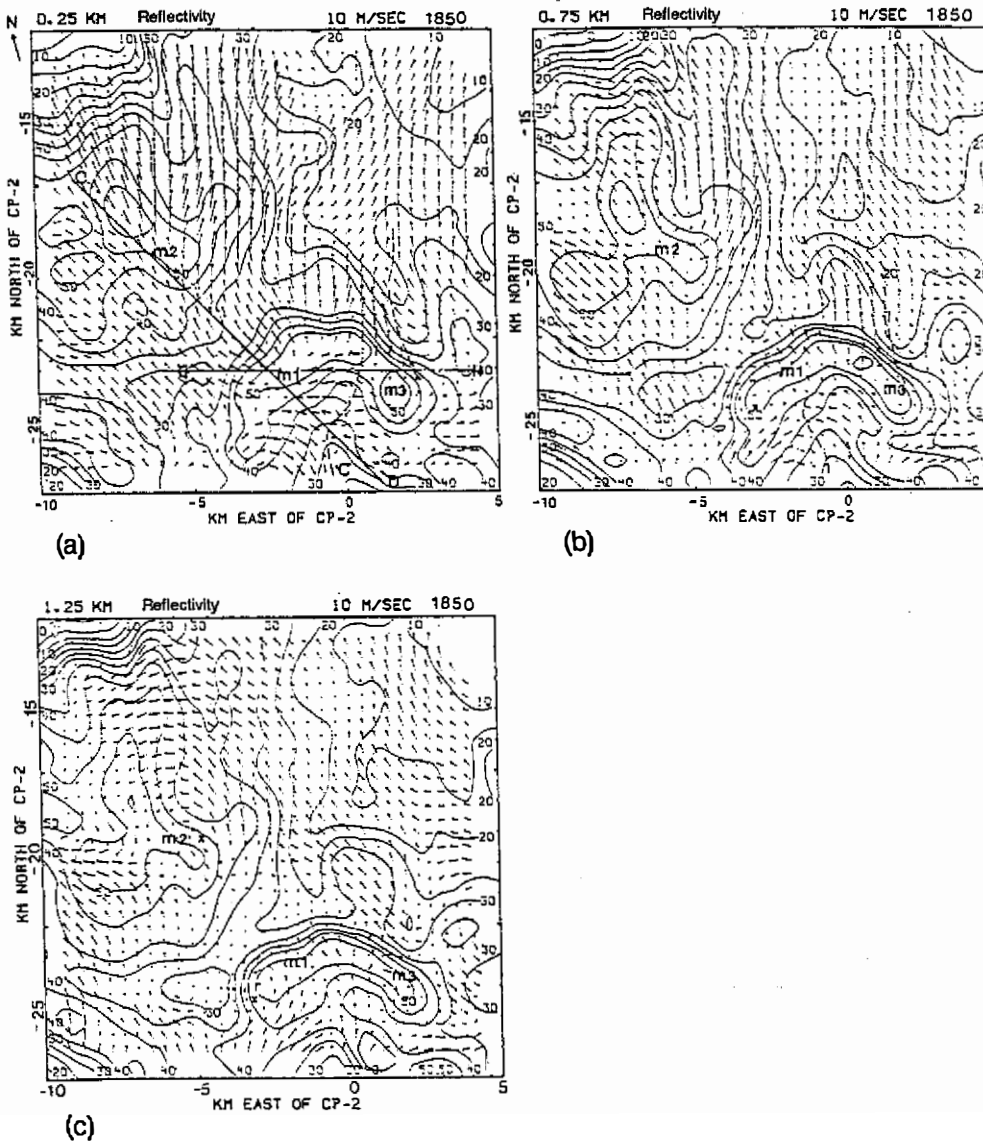
Fig. 5. Same as Fig. 4, except for 1850 MDT. Line CD in panel (a) signify the cross section presented in Figs. 12 to 13.

the flow pattern undergoes some subtle but significant changes as compared to that observed five minutes earlier (Fig. 4a). The major change is attributed to the appearance of M3 at the eastern tail end of the bow echo associated with M1. The center of M3, located at (1.5, −23.5), is embedded within the 50 dBZ reflectivity contour, indicative of precipitation processes. The GF (dashed line) is quite evident, but it is bridged by M3 at its middle point. The presence of M3 has forced the cyclonic grye (c) southeast along the GF to the sourthern edge of the domain near (0, −26). The area of greatest cyclonic shear combined with interaction with warm, buoyant environmental air occurs at this

point. The gyre is in a weaker state of organization. Similar to 1845 MDT, the M2 microburst remains embedded within the high-reflectivity core and is influenced by the outflow of M1 and the environmental flow. There is a strong flow of air toward lower reflectivity values from M2 and M1. This shows that precipitation cooled air is flowing toward the north from M2, undercutting the buoyant environmental air. Recall from the discussion for 1845 MDT at higher levels (Fig. 4c), the 1.25 *km* flow is opposite in direction and is toward the high-reflectivity values from the north.

The 0.75 *km* wind and reflectivity pattern (Fig. 5b) shows the dominance of the environmental flow. As during the 1845 MDT case (Fig. 4b), the flow in the inflow region southeast of M1 and northwest of M2 is almost parallel to the reflectivity contours, except at the northern fringe of the M2 inflow. The GF appears to maintain its structure at this height; whereas, at 1845 MDT, it had largely disappeared. The GF is apparently strengthened, even at higher levels, by the growth of the M3 microburst. Unlike at 1845 MDT, the misocyclone (x) has appeared at the head of the bow echo near M1 at $(-3, -24.5)$. The descent of the misocyclone to 0.75 *km* from the levels above indicates that the microburst system has intensified at 1850 MDT. The presence of greater reflectivity suggests that as the reflectivity core descends, and the system spins up, the misocyclone can extend to lower levels because the spin up compresses the circulation.

At 1.25 *km* (Fig. 5c), the reflectivity pattern remains very similar to that at 0.75 *km*. Three microbursts are still embedded within the high-reflectivity regions with $Z > 50$ *dBZ*. The misocyclones are well organized at this level. The head of the M1 bow echo contains a well-defined misocyclone (x) at $(-3, -24.5)$. Even the M2 microburst has developed a well-defined misocyclone (x) to its east at $(-5, -19)$. The increased organization of the microbursts, coupled with the increased value of downward motion and the previously noted descent and compression of the misocyclone, suggests that the spin up of the misocyclone parallels the increase in intensity of the surface layer microburst. The microburst systems are therefore intensifying. In addition, the source region of dry environmental inflow into M2 now includes environmental air from the northeast of the misocyclone circulation. The reflectivity pattern is evolving from an amorphous triangular region at 1845 MDT to a bow-shaped reflectivity return. The strong inflow winds to the rear of the bow echoes (south for M1 and east for M2) diminish as they cross the reflectivity gradient. The wind emerges on the other side at only a fraction of its former magnitude. There must be a momentum and kinetic energy transfer downward in the downdrafts to account for this discrepancy. In a separate paper, Lin and Coover (1990) examined this point in detail.

4.2 Horizontal Distribution of Vertical Velocity

Figure 6 displays isotachs of vertical velocity at 0.5 and 1 km for 1845 MDT. At 0.5 km (Fig. 6a), upward motion (hatched) prevails along the GF, while downward motion dominates in the microburst regions. The M1 microburst center matches well with the -2 m/s contour. A value of -1 m/s vertical motion, associated with M2, is removed from the region of highest reflectivities, and is displaced downward from the combined mean flow and outflow from M1 as the outflow from M1 overwhelms M2's divergent structure. The maximum divergence is thus shifted to the downwind side of M2. An important characteristic of the w field is that it clearly delineates M1 and M2. Both M1 and M2 are located in an area of sinking motion. A ring of upward motion virtually surrounds M1 and M2, even in the area between M1 and M2. Such features extend to the 1 km level (Fig. 6b) with much stronger upward and downward motions. The vortex center of a cyclonic circulation (c) along the GF is located at $(-1, -24.5)$, which slightly tilts toward the northwest compared to that at 0.5 km due to the effect of environmental flow. Once again, both M1 and M2 are in the regions of downward motion. Centers of the downdrafts match well with the high-reflectivity cores, indicative of the importance of precipitation loading in maintaining the downdrafts and the microbursts at low levels. The misocyclone's circulation center (x), associated with M2, is located at $(-5.5, -18.5)$ and is in the area of strong downward motion ($w < -2$ m/s). Similarly, the circulation center of the M1 misocyclone, located at $(-2.5, -23.5)$, is also
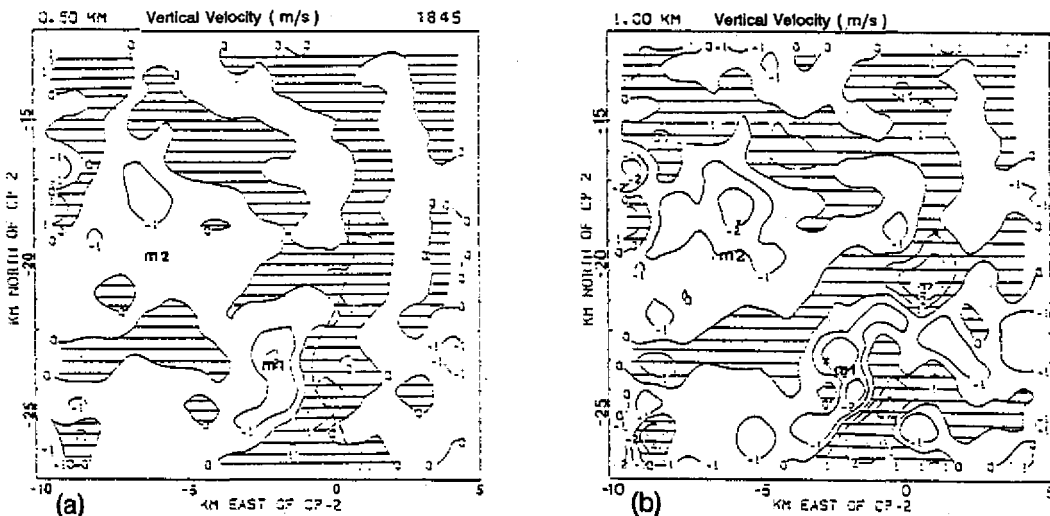

Fig. 6.   The distribution of vertical velocity in meters per second for 1845 MDT at (a) 0.5, and (b) 1 km. Contour interval is 1 m/s with positive values hatched. Centers of the microbursts at 0.25 km are marked. The dashed line represents the gust front (GF).

in the area of maximum downdraft speed $(w < -2\ m/s)$. These produced M1
and M2 at low levels, are governed by the misocyclones which exhibit a distinct
cyclonic rotation. Such features were not observed in the simple case, Lin and
Hughes (1987).

Fields of vertical velocity at 0.5 and 1 km for 1850 MDT are displayed in
Fig. 7. At 0.5 km (Fig. 7a), the w features the bow echo containing M1 and
M3, having a maximum value of $-2\ m/s$ near the M1 microburst. An updraft
velocity of 2 m/s is associated with the GF between M1 and M3. This value
is double the value for 1845 MDT (Fig. 6a). The M1 downdraft has the same
magnitude as 1845 MDT, but M3 is assisting in making the bow echo an area
of downward motion. A semi-circle of downward motion surrounds the updraft.
The intensification of convergence and upward motion near the GF appears
due to M3's intensification. While the microburst M2 is not obvious from the
horizontal wind pattern, it is more apparent from the w pattern. Notice how
M2 is separated from M1 and M3 by an area of upward motion between the
two systems. M2 was not classified as a separate system by storm cataloguers
based on the horizontal wind shear requirements for a microburst (Wilson *et
al.*, 1984). It is apparent from the w field that two distinct centers of downward
motion are present, which correspond well to the high reflectivity cores. The
result suggests that the present convention of classifying microbursts is based on
the singular, isolated microburst event. A broader definition based on the total
storm structure to include the vertical velocity field may prove more accurate.
At 1 km (Fig. 7b), the w field depicts that the bow echoes are elongated areas
of downward motion. The microbursts are surrounded by areas of upward
motion caused by gust fronts and other convergence zones. The magnitude of

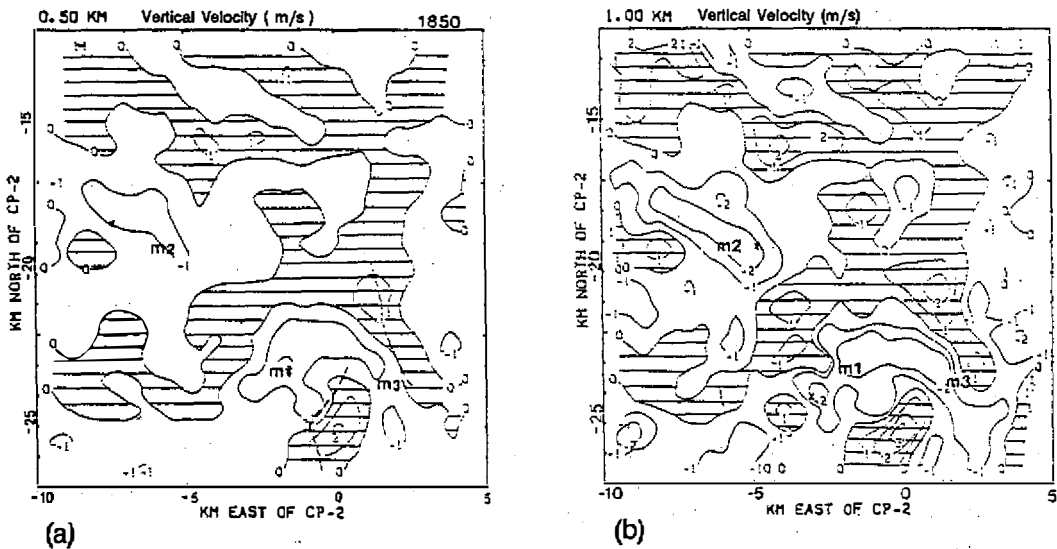(a)   (b)

Fig. 7.   Same as Fig. 6, except for 1850 MDT.

the updrafts and downdrafts has increased from the values presented at 1845 MDT (Fig. 6b). Note that two centers of the misocyclones, located at $(-3, -24)$ and $(-5, -19)$ for M1 and M2, respectively, are in the areas of maximum downward motion $(w < -2\ m/s)$ in agreement with those presented at 1845 MDT (Fig. 6b).

4.3   Horizontal Distribution of Deviation Perturbation Pressure

As described in Section 3, values of the deviation perturbation pressure (P'_d) at a given height were recovered from the Doppler derived winds using the horizontal pressure Eq. (4). Momentum checks were then performed to estimate the relative errors, E_r, in pressure retrievals. Values of momentum checks range from 0.20 to 0.40, indicating a good balance between the horizontal perturbation-pressures gradients and the horizontal accelerations of airflow.

The retrieved P'_d fields in hPa (mb) for both analysis times at 0.5 km are presented in Fig. 8. In the displays, storm-relative winds are superimposed. Notice that the horizontal flow pattern is quite similar in character to that at 0.25 km presented earlier. Features such as the GF, microburst outflow, and cyclonic circulation are also found at this level for both times. At 1845 MDT (Fig. 8a), high pressure occurs in the microburst areas, while low pressure is located along the GF and generally surrounds the microbursts. This finding is consistent with that reported in Lin *et al.* (1987) and Lin and Hughes (1987) for the simple case. A pronounced horizontal perturbation-pressure gradient is generally required to balance the microburst diverging outflow at low levels. The mesocyclone-like vortex (c) on the GF noted earlier has low pressure due
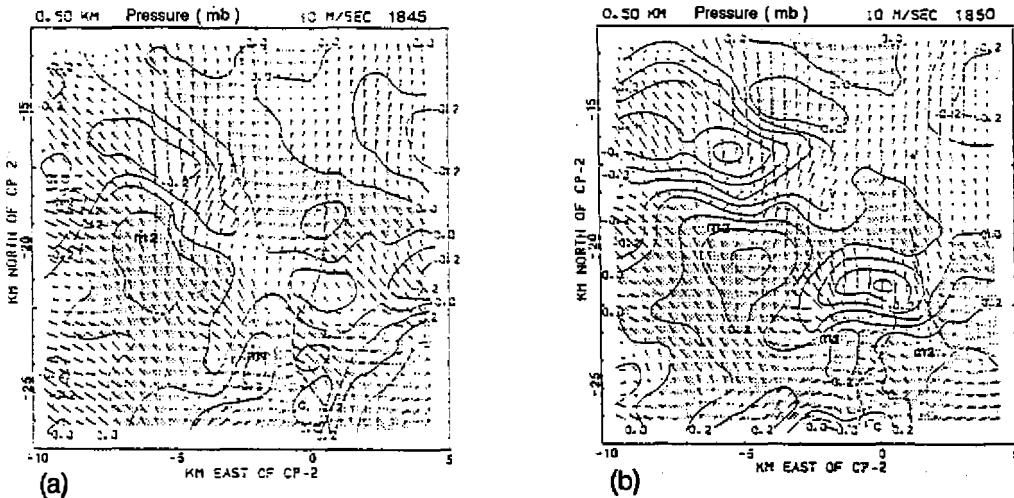

Fig. 8.   The distribution of deviation perturbation pressure in hPa (mb) for (a) 1845, and (b) 1850 MDT at 0.5 km. Contour interval is 0.1 mb with positive values shaded. Horizontal storm-relative winds are superimposed. Centers of the microbursts at 0.25 km are marked. The dashed line represents the gust front (GF).

to its rotation. Inspection of Fig. 8 further reveals that the retrieved P'_d field as a whole is in agreement with the horizontal flow field.

A similar pressure pattern is observed at 1850 MDT (Fig. 8b). However, horizontal pressure gradients are much stronger than those at 1845 MDT. The difference is attributed to the intensification of M1 and M2, and the appearance of M3 mentioned previously. As the microbursts intensify, the horizontal diverging outflow at low levels also strengthens. As a result, much stronger horizontal pressure gradients are needed in order to balance the stronger diverging outflow.

4.4   Horizontal Distribution of Deviation Virtual Temperature

Horizontal distributions of deviation perturbation temperature (T'_{vd}) for both times at 0.5 km are displayed in Fig. 9. The temperature field is retrieved from the buoyancy Eq. (5) using the information of derived w and vertical perturbation-pressure gradients. Since both quantities are subject to uncertainty, temperature retrieval in general is less reliable than pressure retrieval (Gal-Chen, 1978). Further, the retrieved field is the deviation from its horizontal average rather than the deviation from the environmental temperature at the same height. Therefore caution must be exercised in interpreting the result. At 1845 MDT (Fig. 9a), a broad region of relative cooling $(T'_{vd} < 0)$ is observed in conjunction with M1 and M2. Such cooling is mainly attributed to the evaporation of raindrops in the downdraft. Since downflow air in the downdraft column is relatively weak, embedded raindrops can evaporate fast enough to maintain a moist-adiabatic descent. The maximum cooling occurs at the level where the vertical velocity is reduced to practically zero (Srivastava, 1985). For these reasons, air within the microburst areas will be colder than the surroundings, resulting in a negatively buoyant outflow from the microburst center. Further, a microburst with weak to moderate descending speed, such as the one being investigated in this study, will have a cold core as depicted in Fig. 9. This result is different from that reported in Lin and Hughes (1987) for the simple case, in which a warm core microburst was observed with a strong downflow at low levels. In the regions outside the microbursts, on the other hand, relative warming $(T'_{vd} > 0)$ prevails, especially in the weak reflectivity areas to the north and northeast of M1 and M2. A distinct temperature contrast is found across the GF with warming to its east and southeast. Note that the environmental air enters form the southeast side of the GF at this level.

A quite similar temperature pattern is also observed at 1850 MDT (Fig. 9b). However, horizontal temperature gradients in the vicinity of the microbursts have increased considerably as compared to those at 1845 MDT. This is caused by the intensification of M1 and M2, and the presence of M3 at 1850 MDT described previously.
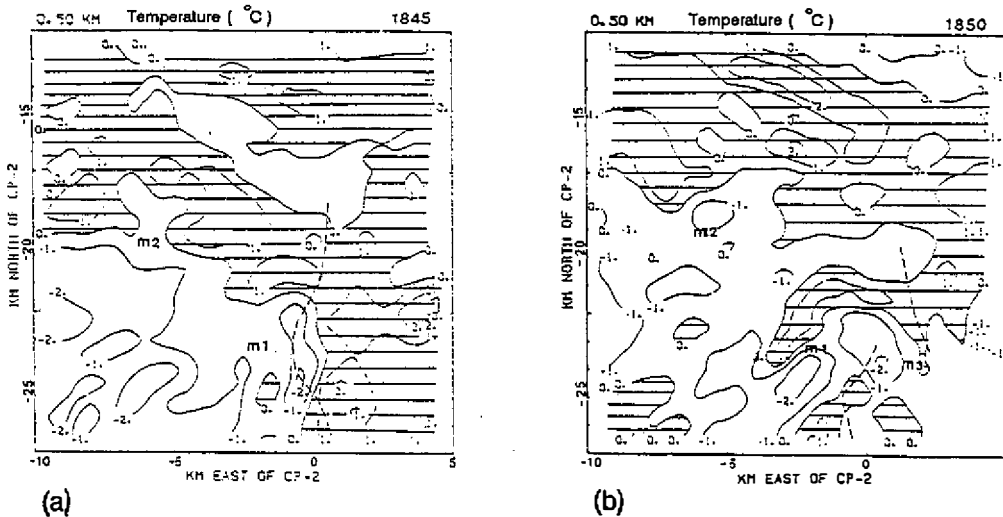
Fig. 9.   Same as Fig. 8, except for deviation perturbation temperature. Contour interval is 1°C with positive values hatched.

4.5   Northwest-southeast Vertical Cross Section

As noted earlier, the retrieved fields of pressure and temperature are the deviations from their horizontal averages rather than the deviations from the environmental means. The unknown area means are still functions of height and will vary from level to level. Hence, vertical cross sections of pressure and temperature must be carefully interpreted with the unknown means in mind. Nevertheless, we found that some useful information of the microburst's dynamics and structure can still be extracted from the cross-sectional analyses. Figure 10 depicts fields of reflectivity (Z) in relation to storm-relative wind, and vertical velocity (w) along line AB in Fig. 4a at 1845 MDT. This cross section passes through M2, M1, the GF and the updraft with a cyclonic circulation. The flow is generally from the southeast (right) to northwest (left) with an area between $(0, -26)$ and $(-2, -24)$, where the flow forms a (vertical) cyclonic circulation underneath the GF (Fig. 10a). This circulation is the cross-sectional view of the cyclonic vortex (c) shown in Fig. 4a. It is a vortex ring induced by the interaction between the microburst outflow and the environmental inflow. For detail, see studies by Fujita (1985), Lin and Hughes (1987), etc. This interaction results in upward motion in the vicinity of the GF (Fig. 10b). The M1 feature is clearly seen in the w display and is embedded within the high reflectivity region $(Z > 50 \; dBZ)$. This suggests that precipitation loading may have played an important role in the maintenance of the downdraft that produced M1 at low levels. To the northwest of M1 near $(-6, -20)$, some evidence of downward motion exists at higher levels, showing the approximate location of M2. However, the magnitude of downward motion for M2 is much smaller than that for M1 at 1845 MDT. Like M1, M2 is also located in the high-
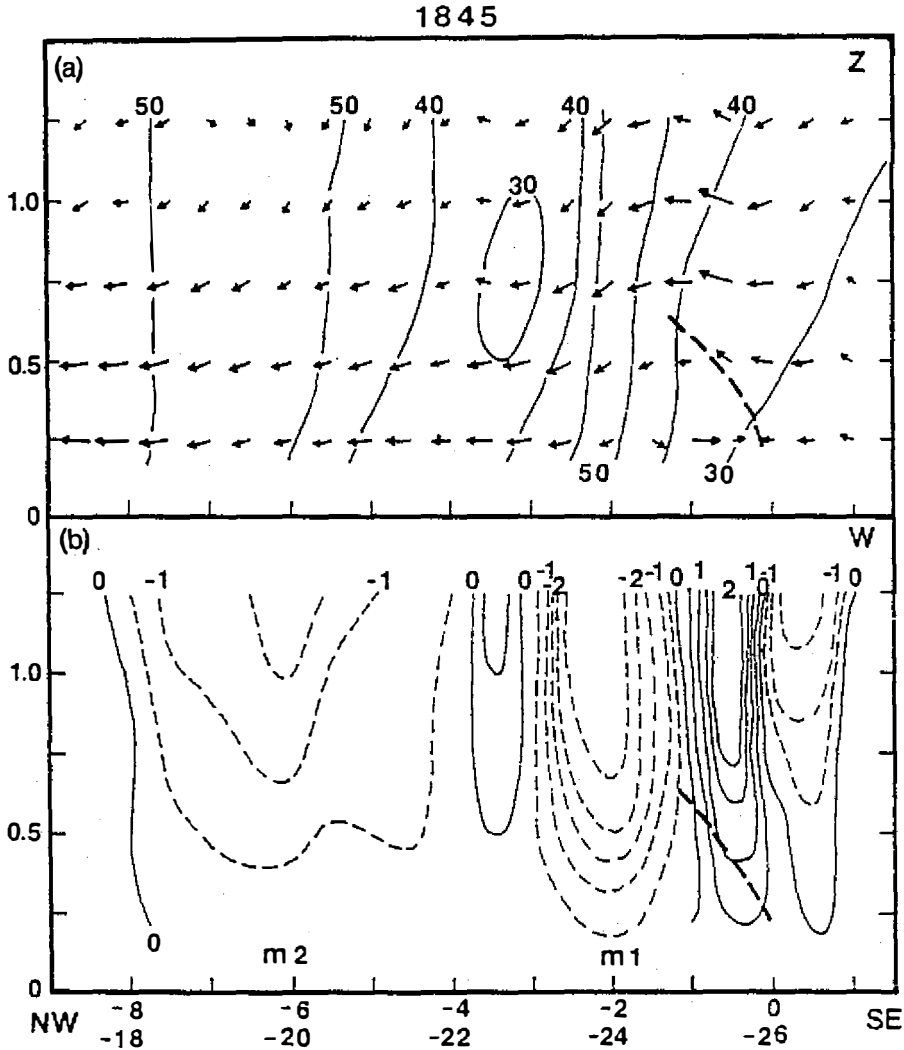
Fig. 10.   Vertical cross sections along line AB in Fig. 4a at 1845 MDT showing fields of
(a) storm-relative wind and reflectivity (Z) in.dBZ, and (b) vertical velocity (w)
in meters per second. Contour intervals are 10 dBZ and 0.5 m/s for Z and w,
respectively, with negative values dashed. Centers of the microbursts near the
surface are marked. The heavy dashed line represents the gust front (GF).

reflectivity core, indicating the importance of precipitation processes in relation
to the microburst occurrence. Between M1 and M2, there is a small region of
upward motion in the relatively weak reflectivity region (Z < 30 dBZ). This
narrow zone clearly separates M1 from M2, illustrating that M1 and M2 are
two separate events under the same storm system.

The pressure calculation (Fig. 11a) reveals that high pressure forms in
the microburst areas with low pressure in the strong outflow regions. This
result is consistent with that reported in Lin and Hughes (1987). Note that the
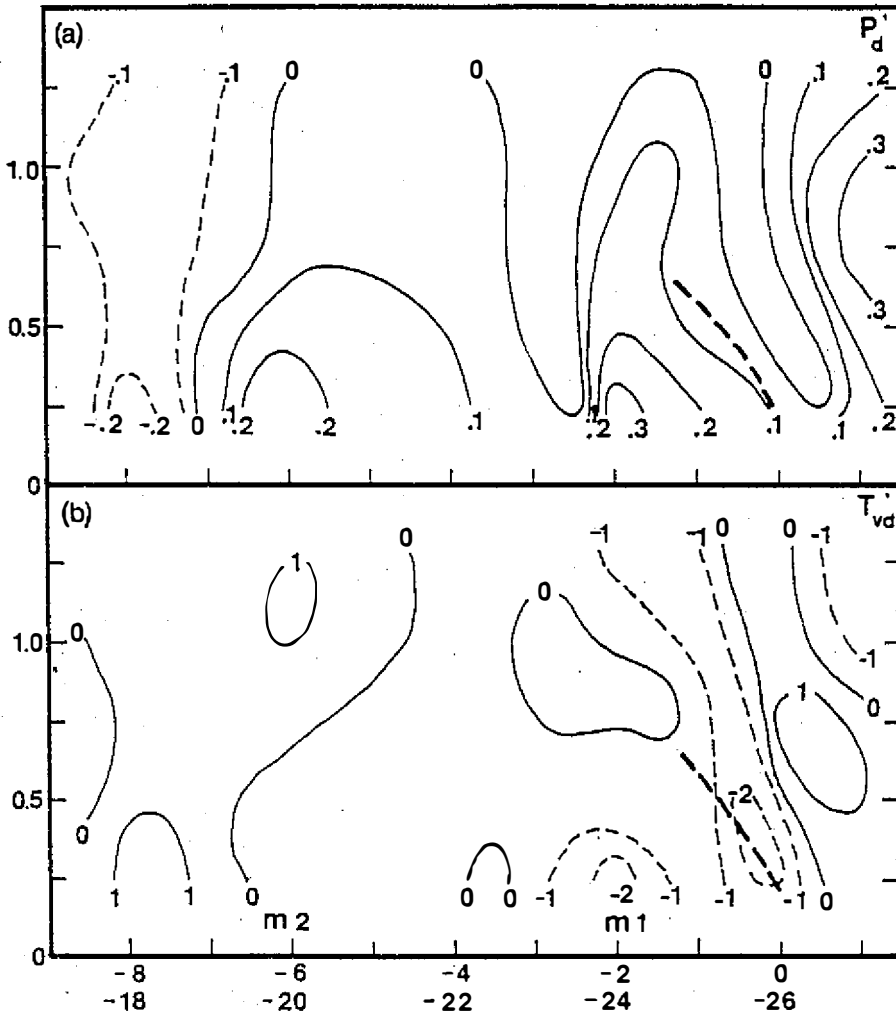
1845

Fig. 11.   Same as Fig. 10, except for (a) deviation perturbation pressure (P_d') in millibars, and (b) deviation perturbation temperature (T_{vd}') in degrees centigrade. Contour intervals are 0.1 mb and 1° for P_d' and T_{vd}', respectively, with negative values dashed.

relationship between the magnitude of diverging outflow and pressure across the microburst was presented in Fig. 4 of Lin and Hughes (1987). The pressure distribution reveals that an area of high pressure on the extreme right side of the cross section accelerates the flow toward an area of relatively weak low pressure near the GF. High pressure forms in the inner region of M1 at $(-2, -24)$. Horizontal pressure gradients are directed from the high pressure center toward the right and left to balance the strong diverging outflow associated with M1 at low levels. In the same manner, the descending motion of M2 results in high pressure inside the microburst core at $(-6, -20)$ with low pressure on its left $(-8, -18)$. A strong horizontal pressure gradient (approximately

0.2 mb/km) develops from M2 to its left toward the northwest in balance with the northwestward outflow over that region. The temperature pattern (Fig. 11b) also reveals some interesting features. The air to the right of the GF is warm environmental air from the southeast. As the warmer air collides with the negatively buoyant outflow of M1 near (0, −26), the GF forms which in turn forces the buoyant environmental air upward. The lifted air rapidly rises and adiabatically cools to form a cold pocket (−2° C) up to 0.5 km. As the flow becomes more horizontal northwest of the most intense cooling, the cooling is reduced and the cold pocket in conjunction with the descending air occurs. As the air approaches the surface, the flow becomes more horizontal and the downward velocity weakens until a cool anomaly (−2° C) is formed near the ground, due to evaporative cooling of the slowly descending air. A similar pattern also occurs in M2 except the cooling at low levels is much weaker. This is attributed to the fact that M1 is more intense than M2 at the time of analysis (see Figs. 10 and 11 for comparison).

Figures 12 and 13 show the northwest-southeast cross section along line CD in Fig. 5a at 1850 MDT. This cross section also passes through M2, M1, the GF, and the updraft with a cyclonic circulation noted earlier. Notice that patterns of the storm-relative wind and reflectivity (Fig. 12a) resemble those at 1845 MDT. However, the microbursts, M1 and M2, have intensified considerably with much stronger downward motion (Fig. 12b). In particular, M2 shows a drastic increase in magnitude from −1.5 to −3 m/s near the 1.25 km level. In the downdraft column, a downward transport of mass is enhanced, causing a mass accumulation near the surface. This, in turn, results in larger high pressure (0.3 mb) in M2 (Fig. 13a). It is surrounded by low pressure to its left (−0.3 mb) and right (−0.1 mb). A much stronger horizontal pressure gradient, up to 0.3 mb/km, is from the center of M2 to the northwest in support of the strong outflow over that region. In the same manner, high pressure also forms in M1 with relatively weak low pressure to its right and left. Pronounced horizontal pressure gradients are directed outward from the center of M1 to maintain the microburst outflow seen in Fig. 12a. The temperature pattern (Fig. 13b) also exhibits some structural changes of M1 and M2 at this time. The intensification of M2 results in the temperature deficit (−1° C) in the microburst area, and the temperature excess (2° C) in the outlying area. A strong horizontal temperature gradient (about 2° C/km) is observed across M2 in conjunction with the strong horizontal pressure gradient noted earlier. The cooling is primarily caused by evaporation in the downflow air. A similar feature is also found in M1 except the horizontal temperature gradient is weaker.

5. CONCLUSIONS

The Doopler derived winds and the retrieved thermodynamic variables
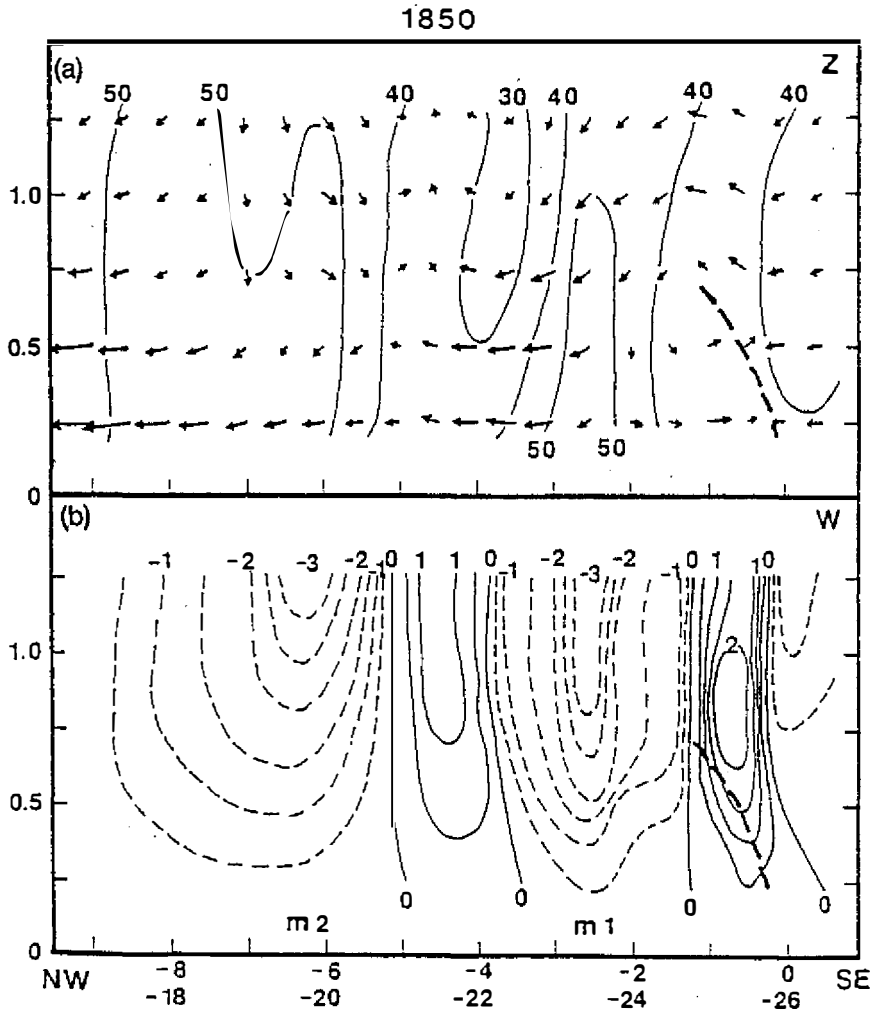
1850

Fig. 12.   Vertical cross sections along line CD in Fig. 5a at 1850 MDT showing fields of (a)
            storm-relative wind and reflectivity (Z) in *dBZ*, and (b) vertical velocity (*w*) in
            meters per second.

were used to study the kinematic, dynamic and thermodynamic structures of a
multiple microburst-producing storm in Colorado. Results show that:

(1) A mesocyclone-like circulation occurs in the vicinity of the GF where the
     environmental wind and horizontal wind shear are a maximum.

(2) A misocyclone circulation may occur above the microburst at levels above
     0.7 *km* in the downdraft column. It intensifies in unison with the bow
     echo. The rotation head of the bow echo is coincident with the misocy-
     clone.

(3) The mesocyclone-like vortex on the GF interacts with the misocyclone to
     feed dry environmental air into the misocyclone circulation, which in turn
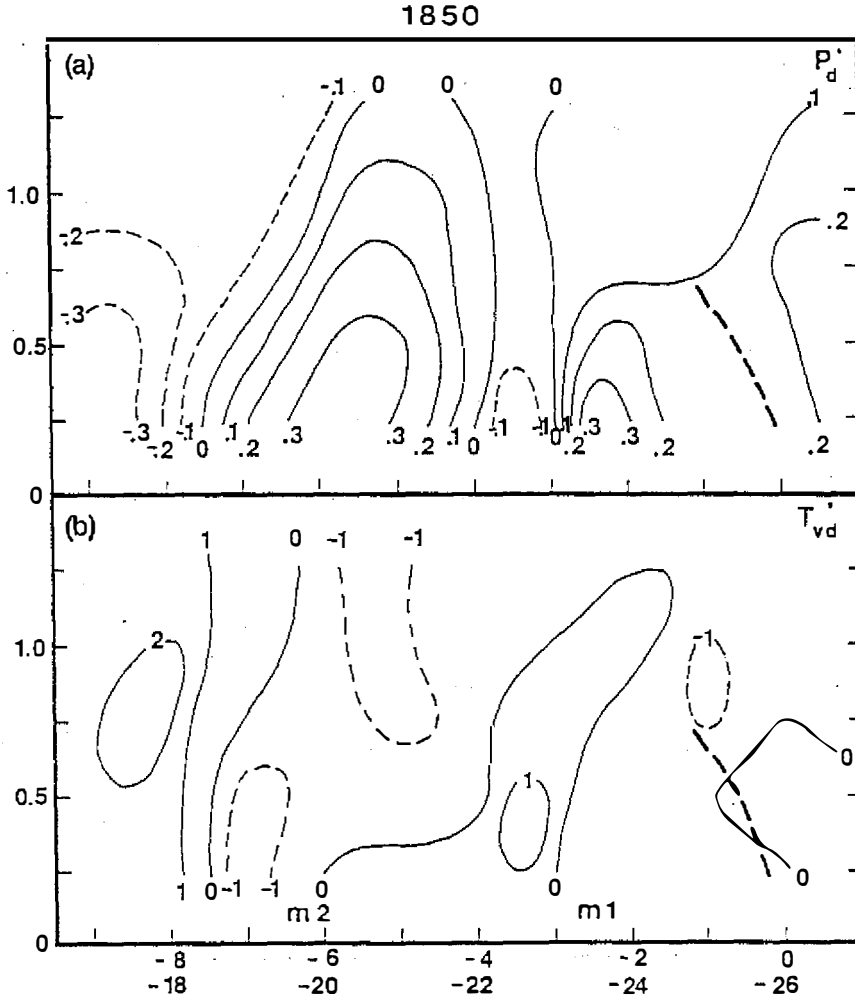
Fig. 13.   Same as Fig. 12, except for (a) deviation perturbation pressure (P_d') in millibars, and (b) deviation perturbation temperature (T_{vd}') in degrees centigrade.

assists in entraining and mixing dry environmental air with the saturated downdraft.

(4) The downdraft that produced a microburst at low levels matches well with the high-reflectivity core, indicative of the importance of precipitation loading in maintaining a downflow.

(5) The retrieved pressure and temperature fields are consistent with the storm's flow field and updraft-downdraft structure. High pressure forms in the microburst inner core with low pressure in the surrounding strong wind areas. Pronounced horizontal pressure gradients develop across the microburst to balance the diverging outflow at the lowest levels.

(6) The wet microburst with a weak downflow will have a cold core since the evaporation of raindrops cools the air more effectively, especially in

the area where the vertical velocity is very small or nearly zero. Conversely, the wet microburst with a strong downflow will have a warm core structure.

REFERENCES

Armijo, L., 1969: A Theory for the Determination of Wind and Precipitation Velocities with Dual-Doppler Radars, *J. Atmos. Sci.*, **26**, 570–573.

Barnes, S., 1973: Mesoscale Objective Analysis Using Weighted Time Series Observations, *NOAA Tech. Memo.*, ERL-NSSL-62, 60 pp. (Available from National Severe Storms Laboratory, Norman, OK, 73069.)

Cressman, G. P., 1959: An Operational Objective Analysis System, *Mon. Weather Rev.*, **87**, 367–374.

Elmore, K. L., J. McCarthy, W. Frost, and H. P. Chang, 1986: A High Resolution Spatial and Temporal Multiple Doppler Analysis of a Microburst and Its Application to Aircraft Flight Simulation, *J. Climate Appl. Meterorol.*, **25**, 1398–1425.

Fujita, T. T., 1985: The Downburst Microburst and Macroburst, *University of Chicago Press*, Chicago, 122 pp.

Gal-Chen, T., 1978: A Method for the Initialization of the Anelastic Equations: Implications for Matching Models with Observations, *Mon. Weather Rev.*, **106**, 587–606.

Gal-Chen, T., and C. E. Hane, 1981: Retrieving Buoyancy and Pressure Fluctuations from Doppler Radar Observations: A Status Report, Progress in Radar Meteorology, *Atmospheric Technology*, NCAR, **13**, 98–104.

Klemp, J. B., and R. B. Wilhelmson, 1978: The Simulation of Three-Dimensional Convective Storm Dynamics, *J. Atmos. Sci.*, **35**, 1070–1096.

Lin, Y. J., and R. G. Hughes, 1987: Structural Features of a Microburst-Producing Storm in Colorado Revealed by JAWS Dual-Doppler Radars, *J. Atmos. Sci.*, **44**, 3640–3655.

Lin, Y. J., R. G. Hughes, and R. W. Pasken, 1987: Subcloud-Layer Kinematic and Dynamic Structures of a Microburst-Producing Thunderstorm in Colorado Determined from JAWS Dual-Doppler Measurements, *Boundary-Layer Meteorol.*, **39**, 67–86.

Lin, Y. J., and J. A. Coover, 1990: Momentum and Eddy Kinetic Energy Transports by a Multiple Microburst-Producing Storm, *J. Geophy. Res.*, **95**, 7625–7636.

Nelson, S. P., and R. A. Brown, 1987: Error Sources and Accuracy of Vertical Velocities Computed from Multiple-Doppler Radar Measurements in Deep Convective Storms, *J. Atmos. Oceanic Technol.*, **4**, 233–238.

Roux, F., J. Testud, M. Payen, and B. Printy, 1984: West African Squall-Line Thunderstorm Structure Retrieved from Dual-Doppler Radar Observations, *J. Atmos. Sci.*, **41**, 3104–3121.

Srivastava, R. C., 1985: A Simple Model of Evaporatively Driven Downdraft: Application to Microburst downdraft, *J. Atmos. Sci.*, **42**, 1004–1023.

Wilson, J. W., R. D. Roberts, C. Kessinger, and J. McCarthy, 1984: Microburst Wind Structure and Evaluation of Doppler Radar for Airport Wind Shear Detection, *J. Climate Appl. Meteorol.*, **23**, 898–915.

產生微爆雷雨系統之觀測研究
（一）運動，動力及熱力結構

林永哲　　　William E. McNamee　　　John A. Coover, Jr.

美國聖路易大學　地球與大氣科學系

美國空軍氣象勤務中心

摘要

　　本文將討論在 JAWS 實驗期間， 1982 年 8 月 5 日在美國科羅拉多州一場發生多重微爆雷雨的運動，動力及熱力結構。分別選取在丹佛市史坦普敦國際機場所收集之三個時間（ 1845， 1847 及 1850 MDT ）之雙都普勒雷達資料，以分析其三度空間風場。

　　涵蓋了此三個微爆系統的分析區域，水平尺度為 15 公里見方，垂直方向自 0.25 公里至 1.25 公里分為五層。水平間距 0.5 公里，垂直間距 0.25 公里。垂直速度以非彈性連續方程式由地面向上積分而得。並由所得三維風場透過動量方程式反求擾動壓力及渦度場。這些場並經過檢驗，確認反求場與風場之間彼此能配合。

　　結果顯示微爆處於高回波降水區內，有一漥微爆伴隨 0.75 公里高度之上一個小型中尺度氣旋（ misocyclone ）中的下降氣流而生。微爆緩慢下降時，因蒸發冷卻作用，而在底層形成一個冷核心，在陣風鋒面附近，環境暖而乾的空氣與下沈之微爆外流相交之處，發展出一個類似中尺度氣旋的環流。高壓在微爆之內部形成，低壓則處於強風區內。水平壓力梯度由微爆中心指向外圍以平衡該區向外快速加速之風場。

　　反求之熱，動力場和風場頗為一致。由小型中尺度氣旋（ misocyclone ）擾動壓力梯度，負浮力及降水負動等諸項合成的作用，是維持在邊界層內微爆之機制。